Influence of Molecular Weight on the Organic Electrochemical Transistor Performance of Ladder-Type Conjugated Polymers

Han-Yan Wu, Chi-Yuan Yang, Qifan Li, Nagesh B. Kolhe, Xenofon Strakosas, Marc-Antoine Stoeckel, Ziang Wu, Wenlong Jin, Marios Savvakis, Renee Kroon, Deyu Tu, Han Young Woo, Magnus Berggren, Samson A. Jenekhe, and Simone Fabiano**

Organic electrochemical transistors (OECTs) hold promise for developing a variety of high-performance (bio-)electronic devices/circuits. While OECTs based on p-type semiconductors have achieved tremendous progress in recent years, n-type OECTs still suffer from low performance, hampering the development of power-efficient electronics. Here, it is demonstrated that fine-tuning the molecular weight of the rigid, ladder-type n-type polymer poly(benz-imidazobenzophenanthroline) (BBL) by only one order of magnitude (from 4.9 to 51 kDa) enables the development of n-type OECTs with record-high geometry-normalized transconductance ($g_{m,norm} \approx 11$ S cm^{-1}) and electron mobility × volumetric capacitance ($\mu C^* \approx 26$ F cm^{-1} V^{-1} s^{-1}), fast temporal response (0.38 ms), and low threshold voltage (0.15 V). This enhancement in OECT performance is ascribed to a more efficient intermolecular charge transport in high-molecular-weight BBL than in the low-molecular-weight counterpart. OECT-based complementary inverters are also demonstrated with record-high voltage gains of up to 100 V V^{-1} and ultralow power consumption down to 0.32 nW, depending on the supply voltage. These devices are among the best sub-1 V complementary inverters reported to date. These findings demonstrate the importance of molecular weight in optimizing the OECT performance of rigid organic mixed ionic–electronic conductors and open for a new generation of power-efficient organic (bio-)electronic devices.

1. Introduction

Organic mixed ionic–electronic conductors (OMIECs) are an emerging material technology for many (opto-)electronic and energy harvesting/storage applications.[1] In OMIECs, the strong coupling between ions and electrons enables efficient charge storage and signal transduction.[2] For this reason, OMIECs have found applications in electrochromic displays,[3] light-emitting electrochemical cells,[4] supercapacitors/batteries,[5] sensors,[6] thermoelectrics,[7] and actuators,[8] to name just a few. When implemented as the active channel materials in organic electrochemical transistors (OECTs),[9] OMIECs endow these devices with record-high transconductance, low operational voltage, and high current density.[10] These attributes make the OECTs a promising technology for chemical/biological sensing,[11] medical diagnostics,[12] large-scale printable circuits,[13] and neuromorphic computing.[14]

H.-Y. Wu, C.-Y. Yang, Q. Li, X. Strakosas, M.-A. Stoeckel, W. Jin, M. Savvakis, R. Kroon, D. Tu, M. Berggren, S. Fabiano
Laboratory of Organic Electronics
Department of Science and Technology
Linköping University
Norrköping SE-60174, Sweden
E-mail: simone.fabiano@liu.se

H.-Y. Wu, R. Kroon, M. Berggren, S. Fabiano
Wallenberg Wood Science Center
Department of Science and Technology
Linköping University
Norrköping SE-60174, Sweden

N. B. Kolhe, S. A. Jenekhe
Department of Chemical Engineering and Department of Chemistry
University of Washington
Seattle, Washington, DC 98195, USA

Z. Wu, H. Y. Woo
Department of Chemistry
College of Science
Korea University
Seoul 136-713, Republic of Korea

M. Berggren, S. Fabiano
n-Ink AB
Teknikringen 7, Linköping SE-58330, Sweden

ADVANCED
SCIENCE NEWS
www.advancedsciencenews.com

ADVANCED
MATERIALS
www.advmat.de

In OECTs, the application of a gate voltage (V_G) enables the penetration of ions from the electrolyte into the OMIEC channel layer. Charges are then accumulated/depleted throughout the entire bulk of the OMIEC layer, with a consequent large variation in the source–drain current (I_D).[15] This volumetric charging/discharging of the OMIEC layer makes the working mechanism of OECTs very different from traditional organic field-effect transistors (OFETs), where charge accumulation/depletion is confined at the semiconductor/dielectric interface.[16] The figures of merit quantifying the efficiency of this ion-to-electron transduction are the transconductance ($g_m = \partial I_D / \partial V_G$) and the product of charge-carrier mobility and volumetric capacitance (μC^*), which are interrelated in the saturation regime according to the equation

$$g_m = \frac{Wd}{L} \mu C^* (V_G - V_{th}) \quad (1)$$

where L is the channel length, W is the channel width, d is the film thickness, μ is the charge-carrier mobility, C^* is the volumetric capacitance, and V_{th} is the threshold voltage. As g_m depends on the volume of the OECT channel material,[17] a geometry-normalized transconductance $g_{m,norm} = g_m \frac{L}{Wd}$ is often used to compare the performance of different OMIECs.

While p-type (hole-transporting) OMIECs can routinely reach $g_{m,norm} > 100$ S cm^{-1} and $\mu C^* > 300$ F cm^{-1} V^{-1} s^{-1} in OECTs,[18] n-type (electron-transporting) OMIECs lag far behind in terms of performance with $g_{m,norm} < 2$ S cm^{-1} and μC^* values of <7 F cm^{-1} V^{-1} s^{-1} (see **Table 1**). This performance mismatch between p-type and n-type OECTs hinders the development of power-efficient complementary devices/circuits, essential to many of the applications mentioned above. Several material and device design strategies, including introduction of oligo(ethylene glycol) side chains,[19] planarization/rigidification of the OMIEC polymer backbone,[20] modification of the source/drain electrode surface,[21] and use of molecular[22] or polymeric[23] dopants, are currently being explored. In the pioneering work by Giovannitti et al.,[24] naphthalenediimide (NDI)-based polymers were functionalized with oligo(ethylene glycol) side chains to yield n-type OECTs with $g_{m,norm} = 0.1$ S cm^{-1} and $\mu C^* = 0.1$ F cm^{-1} V^{-1} s^{-1}. The only modest performance of these NDI-based OECTs was attributed to a low $\mu < 10^{-5}$ cm^2 V^{-1} s^{-1}, most likely due to the highly localized nature of polarons in this class of donor–acceptor polymers.[25] Recently, we suggested that the use of highly planar and rigid conjugated polymers such as the ladder-type poly(benzimidazobenzophenanthroline) (BBL) might help overcome this limitation[26] and demonstrated n-type OECTs with high $g_{m,norm}$ of 0.3 S cm^{-1} and μC^* of 1–2 F cm^{-1} V^{-1} s^{-1}.[27] Remarkably, it was also found that the lack of side chains does not affect the BBL-based OECT's temporal response.[28] This has motivated further research toward developing other rigid conjugated polymers possessing high electron mobility, like those based on fused electron-deficient lactam rings,[20] which own $\mu = 6.5 \times 10^{-3}$ cm^2 V^{-1} s^{-1} and $g_{m,norm} = 0.2$ S cm^{-1}. Despite significant progress, the best n-type OECTs do not yet meet the performance comparable to the p-type counterparts.

An important parameter of conjugated polymers is the molecular weight, which is known to significantly affect their (opto-)

electronic and charge transport properties.[29] In the context of OFETs, charge-carrier mobility is typically found to increase with increasing molecular weight.[30] For example, when the molecular weight of the p-type semiconductor poly(3-hexylthiophene) is increased from 3 to 40 kDa, the field-effect mobility increases by up to four orders of magnitude due to improved connectivity between crystalline regions.[31] Similar trends have been observed for other polymers, such as those based on diketopyrrolopyrrole.[32] Despite the beneficial effect high molecular weight has on the field-effect charge transport properties of conjugated polymers, its role on the OECT electrical characteristics of electrochemically doped OMIECs remains unexplored and poorly understood.

Here, we investigate the influence of molecular weight on the charge transport properties of electrochemically doped BBL and the electrical characteristic of OECTs made thereof. We chose to work with BBL, being this is the best-performing n-type OMIEC for OECTs. We found that increasing the molecular weight of BBL from 4.9 to 51 kDa (i.e., the number of repeating units increases from 15 to 152) enables the development of n-type OECTs with record-high $g_{m,norm}$ (11.1 S cm^{-1}) and μC^* (25.9 F cm^{-1} V^{-1} s^{-1}). We ascribed the observed enhancement in OECT performance to a stronger π–π interaction and higher crystallinity. As a result of a more efficient intermolecular charge transport, high-molecular-weight BBL shows electron mobility over one order of magnitude higher than the low-molecular-weight counterpart, fast transient response down to 0.38 ms, and threshold voltage of 0.15 V. By combining electrochemical analysis, UV–vis spectroelectrochemistry, dynamic light scattering (DLS), and X-ray diffraction data, we quantitatively characterized the impact of molecular weight on energetics, crystallinity, and charge transport properties of BBL. Finally, we demonstrated OECT-based complementary inverters with a record-high voltage gain of up to 100 V V^{-1} and ultralow power consumption down to 0.32 nW, depending on the supply voltage. These devices are among the best performing sub-1 V complementary inverters reported to date. These findings demonstrate the importance of molecular weight to optimize the OECT performance of rigid OMIEC polymers.

2. Results and Discussion

BBL was synthesized by polycondensation reaction of 1,4,5,8-naphthalenetetracarboxylic dianhydride (NDA) and 1,2,4,5-tetraaminobenzene tetrahydrochloride (TABH) in poly(phosphoric acid) (PPA) at high temperature (**Figure 1**a). By controlling the polycondensation reaction time, we obtained BBL with different viscosity-average molecular weights (M_v) of 4.89, 20.0, 32.8, and 50.8 kDa. Based on the M_v, their repeating units were calculated to be 15, 60, 98, and 152 (Figure 1b), so we hereafter refer to BBL$_{15}$, BBL$_{60}$, BBL$_{98}$, and BBL$_{152}$, respectively. Regardless of M_v, these BBL have good solubility in methanesulfonic acid (MSA), and can be spin-cast on different substrates (e.g., gold, silicon, glass, and even polyethylene terephthalate) to form thin films with thickness ranging from 20 to 200 nm. By controlling the BBL-MSA solution concentration (from 1.40 to 7.75 mg mL^{-1}) and spin coating conditions (1000 rpm for 1 min on glass substrates), the BBL film thickness

Table 1. Summary of n-type accumulation-mode OECT performance.

Materials	V_{th} [V]	$g_{m,norm}$ [S cm^{-1}]	τ_{ON} [ms]	I_{ON}/I_{OFF}	μC^* [F cm^{-1} V^{-1} s^{-1}]	Year	Reference
p(gNDI-gT2)	0.28[a]	0.1085	5	3.2×10^3	NA	2016	[24]
BBL	0.21	0.359	900	6.0×10^3	NA	2018	[27]
P-50	0.36[a]	0.067	NA	5.0×10^2	NA	2018	[19]
P-75	0.29[a]	0.141	NA	5.5×10^2	NA	2018	[19]
P-90	0.26[a]	0.21	NA	4.0×10^3	NA	2018	[19]
P-100	0.25[a]	0.204	NA	1.1×10^3	NA	2018	[19]
C60-TEG	0.55	0.0146	80	2.5×10^4	7	2019	[47]
P90, PFBT	0.29	0.0111	NA	NA	0.0008	2019	[21]
P90, MBT	0.27	0.0059	NA	NA	0.0023	2019	[21]
p(NDI-T2-L2)	0.22	0.0084	40[b]	2.2×10^2	0.046	2020	[48]
P-90	0.25	0.0113	NA	1.9×10^2	NA	2020	[22]
P-90:TBAF(10%)	0.25	0.0299	NA	1.7×10^2	NA	2020	[22]
P-90:TBAF(40%)	0.22	0.0905	24	1.2×10^3	NA	2020	[22]
P-90:TBAF(80%)	0.25	0.0833	NA	2.0×10^2	NA	2020	[22]
BBL	0.19	0.815	5.2	1.6×10^3	1.99	2021	[28]
P90	0.24	0.009	41	1.9×10^1	0.0343	2021	[28]
PgNaN	0.37	0.212	127	1.0×10^4	0.662	2021	[20]
PgNgN	0.21	0.007	NA	1.0×10^3	0.037	2021	[20]
p(gNDI-gT2)	0.26	0.13	NA	1.4×10^1	0.06	2021	[49]
p(C3-gNDI-gT2)	0.25	0.34	NA	2.0×10^1	0.13	2021	[49]
p(C6-gNDI-gT2)	0.37	0.37	NA	2.0×10^1	0.16	2021	[49]
p(C$_4$-T2-OMe)	0.46	0.10	NA	NA	0.07	2021	[50]
p(C$_4$-T2-C$_0$-EG)	0.32	0.31	24.6	NA	0.22	2021	[50]
p(C$_4$-T2-C$_2$-EG)	0.30	0.02	6.2	NA	0.01	2021	[50]
p(C$_4$-T2-C$_4$-EG)	0.33	0.01	12.5	NA	0.006	2021	[50]
p(C$_2$-T2)	0.27	0.40	6.3	NA	0.2	2021	[50]
p(C$_4$-T2)	0.24	0.63	7.5	NA	0.3	2021	[50]
p(C$_6$-T2)	0.30	2.28	9.6	NA	1.29	2021	[50]
p(C$_8$-T2)	0.37	0.15	12.7	NA	0.13	2021	[50]
2DPP-OD-TEG	0.89	0.73	500	2.0×10^5	7	2021	[51]
BBL$_{15}$	0.27	0.617	0.89	2.9×10^3	1.94	2021	This work
BBL$_{60}$	0.21	1.92	0.52	8.3×10^4	4.90	2021	This work
BBL$_{98}$	0.18	4.04	0.43	2.0×10^5	10.2	2021	This work
BBL$_{152}$	0.15	11.1	0.38	4.4×10^5	25.9	2021	This work

[a]Calculated from transfer curves; [b]Calculated from transient response.

can be accurately adjusted to be 20.2 ± 1.6 nm for BBL$_{15}$, 19.9 ± 1.3 nm for BBL$_{60}$, 20.2 ± 1.4 nm for BBL$_{98}$, and 20.1 ± 1.2 nm for BBL$_{152}$. UV–vis spectra show that all BBL polymers have two absorption peaks: 1) peak I located at shorter wavelengths (300–400 nm) and ascribed to the n–π^* transition, and 2) peak II located at longer wavelengths (400–800 nm) and ascribed to the π–π^* transition (Figure 1c).[33] The peak II/peak I intensity ratio increases, and the center of peak II redshifts as the number of repeating units increases, suggesting that the effective conjugation length increases as the molecular weight increases.[34] All BBL polymers have a comparable λ_{onset} of about 716 nm,

indicating similar optical bandgaps (E_{gap} = 1.74 eV). As measured by cyclic voltammetry (CV), the lowest unoccupied molecular orbital energy level is estimated to be around −4.38 eV and independent of molecular weight (Figure 1d and Figure S1, Supporting Information). The highest occupied molecular orbital energy level is calculated to be −6.12 eV. For dilute MSA solution (0.02–0.4 mg mL^{-1}), the UV–vis spectra and DLS measurements show that BBL does not form aggregates and is in a single polymer chain regime (Figures S2 and S3, Supporting Information).[35] In addition, the DLS decay rate (Γ) decreases as the number of repeating units increases (Figure 1e and
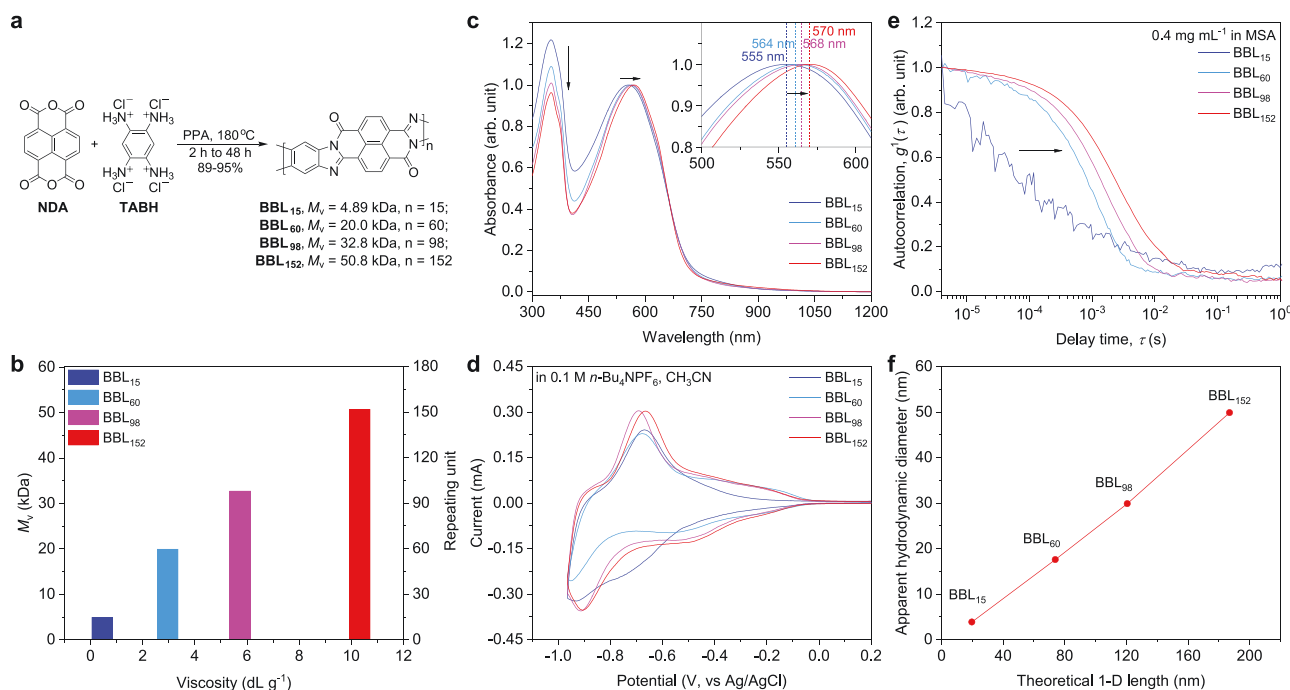
Figure 1. Synthesis and physicochemical properties of BBL. a) Synthetic route, b) viscosity-average molecular weight (M_v) and calculated repeating unit (n) of BBL$_{15}$, BBL$_{60}$, BBL$_{98}$, and BBL$_{152}$. c) UV–vis–NIR absorption spectra of 200 nm thin BBL$_{15}$, BBL$_{60}$, BBL$_{98}$, and BBL$_{152}$ films. Inset: zoom-in of the absorption spectra in the region 500–610 nm. d) CV of BBL$_{15}$, BBL$_{60}$, BBL$_{98}$, and BBL$_{152}$ in 0.1 M n-Bu$_4$NPF$_6$ acetonitrile solution. e) DLS analysis showing normalized first-order autocorrelation function and f) apparent hydrodynamic diameter of BBL$_{15}$, BBL$_{60}$, BBL$_{98}$, and BBL$_{152}$ in methanesulfonic acid (MSA) solutions. The theoretical length of the BBL repeating unit (1.23 nm) is calculated through DFT calculation on a BBL trimer (B3LYP/6-311+g(d,p) level).

Figures S4 and S5, Supporting Information). The apparent hydrodynamic diameters of BBL$_{15}$, BBL$_{60}$, BBL$_{98}$, and BBL$_{152}$ are calculated to be 3.9, 18, 30, and 50 nm, respectively. Interestingly, the apparent hydrodynamic diameter increases linearly with the theoretical 1D length (BBL repeating unit length = 1.23 nm) calculated by density functional theory (DFT, Figure 1f). This suggests that BBL chains retain a semi-rigid character even in solution, and the increase in molecular weight does not lead to a decrease in polymer chain rigidity. Hence, we expect that increasing BBL's molecular weight would result in enhanced charge transport properties.

Grazing-incidence wide-angle X-ray scattering (GIWAXS) was employed to analyze BBL thin-film microstructures when spin-cast from MSA (**Figure 2**a–f). BBL$_{15}$ shows mixed edge-on and face-on bimodal orientation with respect to the substrate, while BBL$_{60}$, BBL$_{98}$, and BBL$_{152}$ present a predominant edge-on orientation. All the BBL polymers show strong lamellar (100) diffraction peak at around $q_z = 0.75$ Å^{-1} (d-spacing = 8.4 Å) and a strong π–π stacking (010) peak at around $q_z = 1.86$ Å^{-1} (d-spacing = 3.4 Å). As the molecular weight increases, the π–π stacking distance slightly decreases from 3.40 Å for BBL$_{15}$ to 3.38 Å for BBL$_{152}$. The moderate decrease in π–π stacking distance is indicative of a stronger π–π interaction in the case of longer BBL polymer chains (Figure 2g,h and Figure S6, Supporting Information). The π–π stacking and lamellar packing crystallinities are also enhanced as the molecular weight increases, as suggested by the longer coherence lengths and lower paracrystalline disorder (Figure 2i,j and Figures S6–S8, Supporting Information). Atomic force microscopy (AFM)

analysis (Figure 2k–n) shows that the spin-cast BBL forms polycrystalline-like thin films, with roughness ranging from 4.87 nm for BBL$_{15}$ to 2.91 nm for BBL$_{152}$. All these results suggest that higher molecular weight of BBL results in stronger π–π interaction, higher crystallinity, and smoother thin films, which could facilitate intermolecular charge transport.

We then performed spectroelectrochemistry measurements to explore how molecular weight affects the electronic band structure (i.e., optical properties) of BBL upon electrochemical doping in 0.1 M NaCl aqueous electrolyte. **Figure 3**a–d shows that all BBL samples can be electrochemically doped at low voltage (<0.7 V vs Ag/AgCl), with a clearly visible ground-state bleaching occurring at 320–375 nm and 440–656 nm, and the formation of two polaron bands at 375–440 nm and 656–1200 nm (see also Figure S9, Supporting Information). This indicates that a positive bias drives sodium ions (Na$^+$) from the electrolyte into the bulk of the BBL films and promotes the injection/accumulation of negative charges into the BBL conjugated polymer backbone. For all BBL batches, the relative absorption intensity of the polaron band induced by electrochemical doping reaches 0.3 a.u. in the thickness-normalized differential absorbance spectra. These significant changes in the electronic band structure of BBL upon electrochemical doping are comparable to those observed by chemical (molecular and polymeric) doping.[23,36] In addition, the formation of polaronic species in BBL$_{15}$ starts at voltage >0.2 V vs Ag/AgCl, while for BBL$_{60}$, BBL$_{98}$, and BBL$_{152}$ it starts already at a lower voltage (Figure 3e,f and Figure S10, Supporting Information).
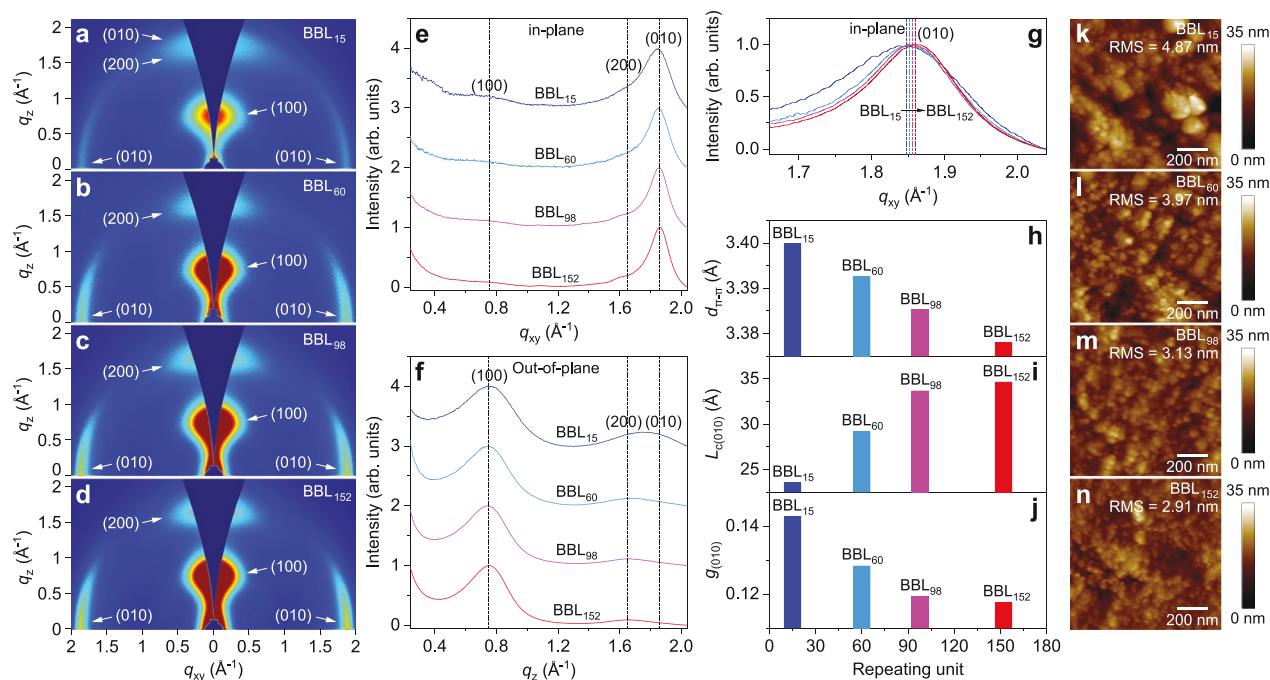
Figure 2. Thin-film microstructures. a–d) 2D GIWAXS patterns of BBL$_{15}$ (a), BBL$_{60}$ (b), BBL$_{98}$ (c), and BBL$_{152}$ (d) thin films. e,f) Out-of-plane (e) and in-plane (f) GIWAXS line cuts of BBL$_{15}$, BBL$_{60}$, BBL$_{98}$, and BBL$_{152}$ thin films. g) Overlap of π–π stacking (010) diffraction peaks of BBL$_{15}$, BBL$_{60}$, BBL$_{98}$, and BBL$_{152}$. h) π–π distance ($d_{\pi-\pi}$) of BBL$_{15}$, BBL$_{60}$, BBL$_{98}$, and BBL$_{152}$. i) Coherence length ($L_{c(010)}$) of BBL$_{15}$, BBL$_{60}$, BBL$_{98}$, and BBL$_{152}$. j) Paracrystalline disorder ($g_{(010)}$) of BBL$_{15}$, BBL$_{60}$, BBL$_{98}$, and BBL$_{152}$. k–n) AFM height images of BBL$_{15}$ (k), BBL$_{60}$ (l), BBL$_{98}$ (m), and BBL$_{152}$ (n) films. The root mean square (RMS) surface roughness is also reported.
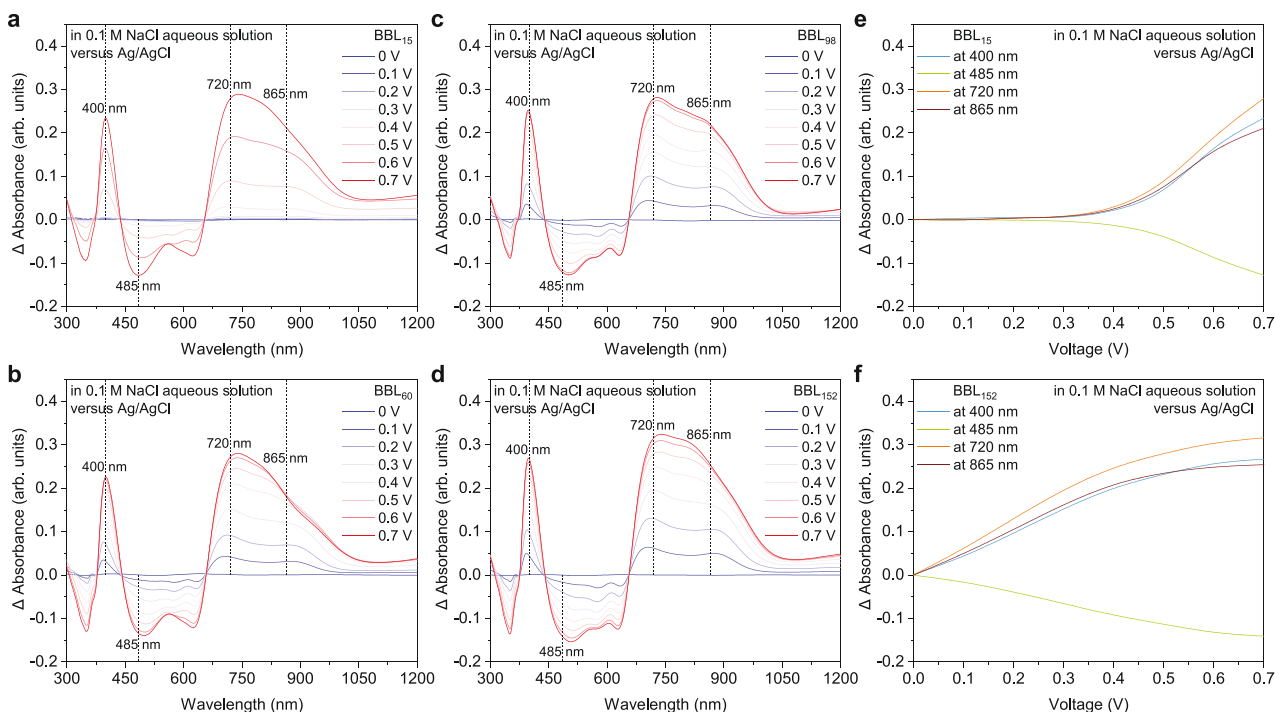
Figure 3. Differential spectroelectrochemistry. a–d) Differential absorption spectra of BBL$_{15}$ (a), BBL$_{60}$ (b), BBL$_{98}$ (c), and BBL$_{152}$ (d) scanned between 0 and 0.7 V versus Ag/AgCl electrode in 0.1 M NaCl aqueous solution. e,f) Differential absorption spectra of BBL$_{15}$ (e) and BBL$_{152}$ (f) at select wavelengths scanned between 0 and 0.7 V versus Ag/AgCl electrode in 0.1 M NaCl aqueous solution. In all the spectroelectrochemistry tests, the BBL films were grounded, and the voltage was applied to the Ag/AgCl electrode, similar to the gate voltage in OECTs.
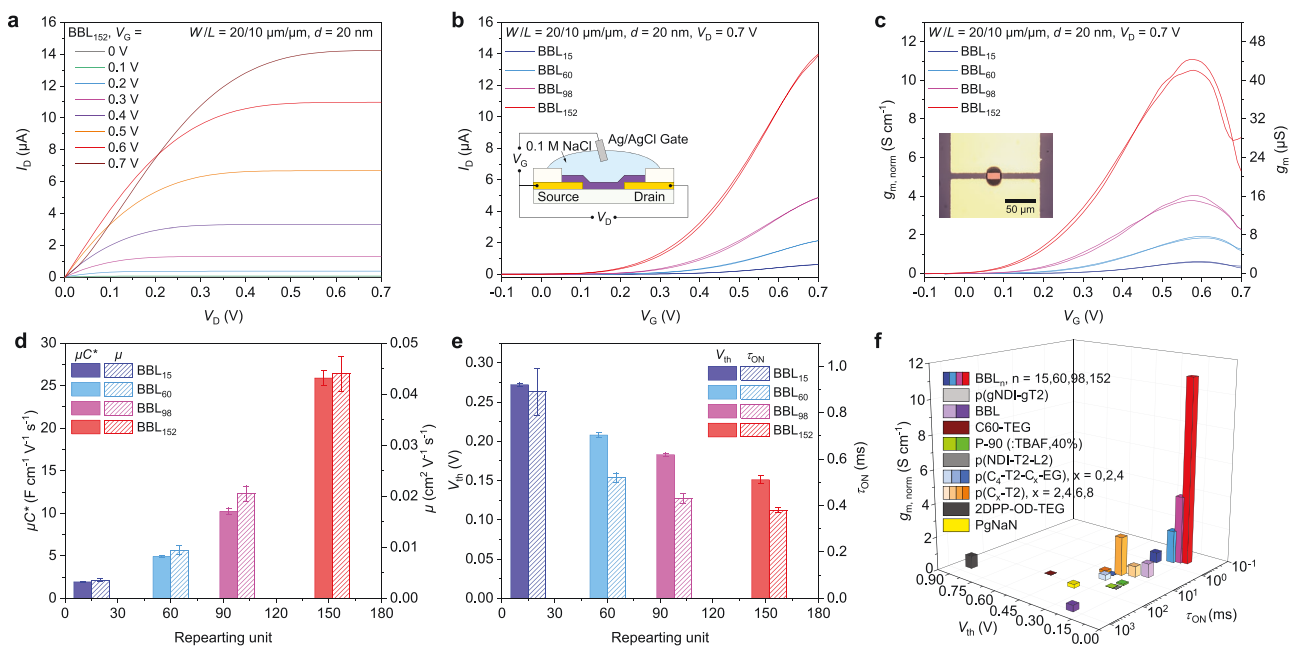
Figure 4. OECT performance. a) Output characteristics of a BBL$_{152}$-based OECT. b) Transfer characteristics of BBL$_{15}$, BBL$_{60}$, BBL$_{98}$, and BBL$_{152}$-based OECTs. Inset: cross-sectional schematic of the OECTs. c) Transconductance (g_m) and geometry-normalized transconductance ($g_{m,norm}$) of BBL$_{15}$, BBL$_{60}$, BBL$_{98}$, and BBL$_{152}$ OECTs. Inset: top-view microscopy photograph of the channel region of a BBL$_{152}$-based OECT. d) μC^* and μ_{OECT} of BBL$_{15}$, BBL$_{60}$, BBL$_{98}$, and BBL$_{152}$, calculated from the OECT transfer characteristics. e) Threshold voltage (V_{th}) and τ_{ON} of BBL$_{15}$, BBL$_{60}$, BBL$_{98}$, and BBL$_{152}$-based OECTs. f) Comparison of V_{th}, τ_{ON}, and $g_{m,norm}$ values with the known n-type accumulation-mode OECTs reported in the literature. All the above BBL$_{15}$, BBL$_{60}$, BBL$_{98}$, and BBL$_{152}$-based OECTs have the same channel geometry ($W = 20$ μm, $L = 10$ μm, $d = 20$ nm). The error bars indicate standard deviation for ten experimental replicates.

Next, we evaluated the OECTs performance of the different BBL batches (**Figure 4**a–f). The OECTs were fabricated following the description reported in the Experimental Section. In brief, gold source/drain electrodes were deposited on glass substrates and coated by a 4 μm-thick parylene layer. Thin BBL films were cast and patterned using another layer of parylene to define the OECT channel length and width ($W/L = 20$ μm/10 μm or 100 μm/10 μm). Finally, a 0.1 M NaCl aqueous solution was used as the electrolyte and an Ag/AgCl pellet was dipped into the electrolyte to serve as the gate electrode (Figure 4b,c, inset graphs). All BBL-based OECTs show typical n-type accumulation-mode output and transfer characteristics, as well as excellent reproducibility with an ON current standard deviation of less than 3% for ten different devices (Figure S11, Supporting Information). The ON/OFF ratio increases from 2.9×10^3 for BBL$_{15}$ to 4.4×10^5 for BBL$_{152}$-based OECTs (Figure 4a,b and Figures S12 and S13, Supporting Information). At $V_D = V_G = 0.7$ V, I_D reaches the maximum value of 0.624 ± 0.018 μA for BBL$_{15}$ and increases up to 14.2 ± 0.3 μA for BBL$_{152}$ (Figure 4b). The max $g_{m,norm}$ increases more than one order of magnitude within the series going from 0.617 ± 0.017 S cm^{-1} for BBL$_{15}$ to 11.1 ± 0.2 S cm^{-1} for BBL$_{152}$ (Figure 4c and Tables S1 and S2, Supporting Information), with the latter being the highest transconductance reported to date for n-type OECTs (see Table 1). Based on the transfer curves reported in Figure S11 in the Supporting Information, we then calculated μC^* to be 1.94 ± 0.05, 4.90 ± 0.16, 10.2 ± 0.4 and 25.9 ± 0.9 F cm^{-1} V^{-1} s^{-1} for BBL$_{15}$, BBL$_{60}$, BBL$_{98}$, and BBL$_{152}$, respectively (Figure 4d). As C^* does not change significantly within the series, with average values in

the range of 500–590 F cm^{-3} (Figure S14, Supporting Information), we estimated an increase of more than one order of magnitude in the electron mobility, with μ_{OECT} values ranging from $(3.59 \pm 0.23) \times 10^{-3}$ cm^2 V^{-1} s^{-1} for BBL$_{15}$ to $(4.40 \pm 0.34) \times 10^{-2}$ cm^2 V^{-1} s^{-1} for BBL$_{152}$ (Figure 4d). This is consistent with the DLS and GIWAXS data, suggesting that a longer rigid polymer backbone with higher crystallinity enhances the BBL charge-transport properties. Interestingly, V_{th} decreases with increasing the molecular weight, going from 0.272 ± 0.002 V for BBL$_{15}$ to 0.151 ± 0.005 V for BBL$_{152}$ (Figure 4e and Figure S13, Supporting Information). Note that the drain current in the linear regime ($V_D < 0.2$ V) decreases at $V_G > 0.6$ V. The observed drain current evolution at high gate voltages is typical of OECTs and commonly ascribed to either contact resistance[21] or drop in mobility at high charge density.[37]

Transient response of the OECTs' drain current plays a crucial role in the development of high-speed (bio-)electronic devices and circuits. The switching speed of BBL-based OECTs was measured by pulsing V_G between 0 and 0.6 V, and measuring the increase/decrease in I_D. The latter was then fitted by using an exponential fit to extract the rise (τ_{ON}) and decay (τ_{OFF}) times. For comparison, we also estimated the OECT's response time by measuring the time that it takes for I_D to reach 90% of its max ($t_{ON,90\%}$) and min ($t_{OFF,90\%}$) value while V_G is pulsed between 0 and 0.6 V. BBL$_{15}$ shows fast transient response with $\tau_{ON} = 0.89 \pm 0.10$ ms ($t_{ON,90\%} = 3.76 \pm 0.36$ ms) and $\tau_{OFF} = 0.70 \pm 0.16$ ms ($t_{OFF,90\%} = 2.36 \pm 0.48$ ms). A twofold increase in switching speed is observed for BBL$_{152}$, with $\tau_{ON} = 0.38 \pm 0.01$ ms ($t_{ON,90\%} = 1.18 \pm 0.03$ ms) and $\tau_{OFF} = 0.15 \pm 0.02$ ms
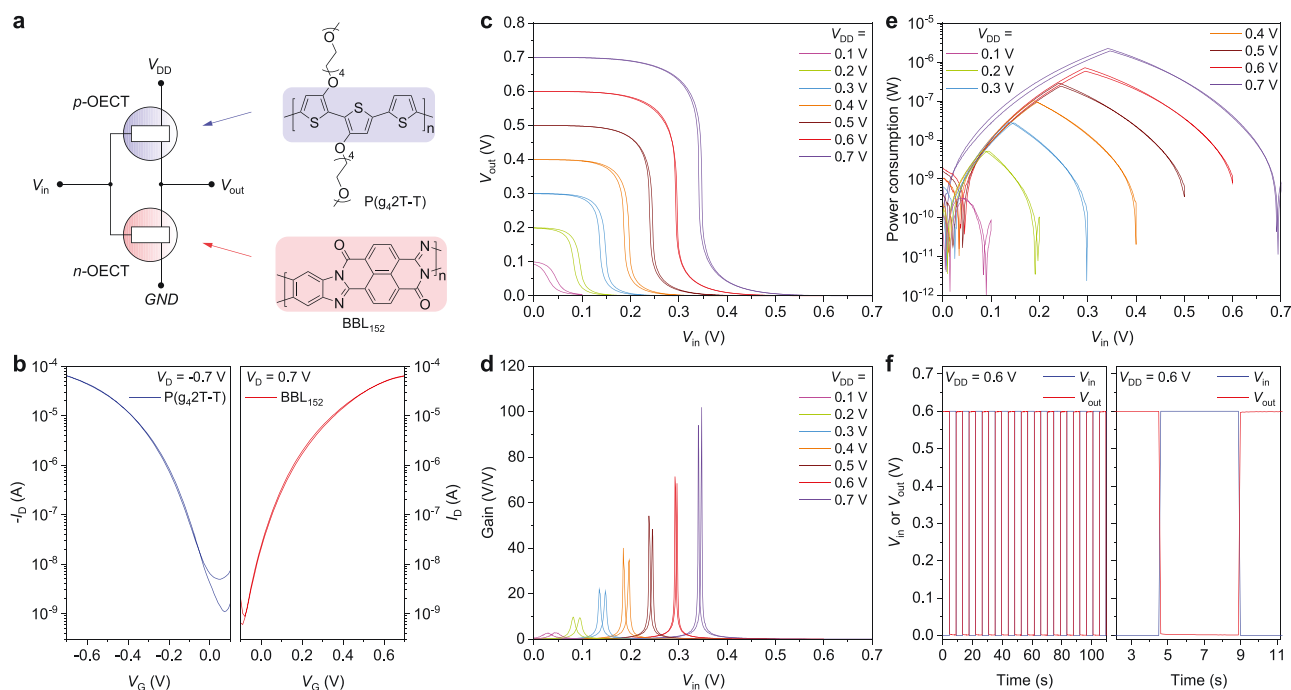
Figure 5. OECT-based complementary inverters. a) Schematic of the complementary inverter and chemical structures of P(g$_4$2T-T) (p-type) and BBL OECT channel materials. b) Transfer curves of P(g$_4$2T-T)-based OECT and BBL$_{152}$-based OECT, showing fully balanced p-type and n-type transport characteristics. c) Typical voltage transfer characteristics (VTC) of the inverter at various supply voltages (from 0.1 to 0.7 V). d) Voltage gain of the inverter at various supply voltages. e) Power consumption of the inverter at various supply voltages. f) Input and output given by the inverter showing "0" and "1" states. In all the above OECTs and inverters, p-type OECTs have channel geometry $W = 100$ µm, $L = 10$ µm, $d = 2.7$ nm, and n-type OECTs have channel geometry $W = 100$ µm, $L = 10$ µm, $d = 20$ nm.

($t_{OFF,90\%} = 0.42 \pm 0.05$ ms) (Figure 4e as well as Figure S15 and Table S6, Supporting Information). Note that the switching speed of the best BBL-based OECTs reported in this study is more than one order of magnitude faster than that recently reported for photolithography-made BBL-based OECTs (5 ms)[28] and 30× faster than the fully printed BBL-based OECTs.[38] All the BBL-based OECTs show exceptionally high stability in air, with their current retentions being larger than 95% for 1000 switching cycles over a period of about 6 h of continuous operation (Figure S16, Supporting Information). OECTs with channel $W/L = 10$ show identical performance to those with channel $W/L = 2$, and the results are presented in Figures S17 and S19 (Supporting Information) and summarized in Tables S1–S3 of the Supporting Information. A comparison of the performance of the BBL$_{15}$–BBL$_{152}$ series and the other n-type accumulation OECT materials reported to date is shown in Figure 4f and summarized in Table 1. BBL$_{152}$ shows the highest transconductance ($g_{m,norm} = 11.1$ S cm^{-1}), fastest transient response ($\tau_{ON} = 0.38$ ms), and lowest threshold voltage ($V_{th} = 0.15$ V).

Having demonstrated n-type accumulation-mode OECTs with record-high performance, we then moved to fabricate complementary accumulation-mode inverters (**Figure 5**a). We used the hole-transporting polythiophene P(g$_4$2T-T)[39] to construct accumulation-mode pull-up (p-type) OECTs in the complementary inverters. P(g$_4$2T-T) shows high ON/OFF ratio of 5.9×10^4, low V_{th} of -0.178 ± 0.02 V, high $g_{m, norm}$ of 80 ± 2 S cm^{-1}, high $\mu C^* = 187 \pm 6$ F cm^{-1} V^{-1} s^{-1}, and fast transient response with $\tau_{ON} = 0.074 \pm 0.001$ ms ($t_{ON, 90\%} = 0.203 \pm 0.003$ ms) and $\tau_{OFF} = 0.025 \pm 0.001$ ms ($t_{OFF, 90\%} = 0.039 \pm 0.002$ ms) (Figure S20,

Supporting Information). To achieve balanced driving strengths of the pull-up and pull-down (n-type) transistors, we set the thickness of P(g$_4$2T-T) and BBL$_{152}$ channel layers to be 2.7 and 20 nm, respectively. A channel geometry of $W/L = 10$ was used for both p-type and n-type OECTs. The pull-up and pull-down OECTs show perfectly balanced electrical characteristics, with comparable current levels even in their sub-threshold region at V_G around ±0.1 V (Figure 5b and Figure S21, Supporting Information). These well-balanced p-/n-type electrical characteristics result in complementary inverters operating at supply voltages (V_{DD}) as low as 0.1 V, with a switching threshold (V_M) of 0.037 V, voltage gain over 2.5 V V^{-1}, static power consumption (P_{static}) of 0.12 nW, and dynamic power consumption ($P_{dynamic}$) of 0.32 nW (Figure 5c–f and Tables S4 and S5 in the Supporting Information). At $V_{DD} = 0.7$ V, V_M approaches the ideal $V_{DD}/2$ (i.e., $V_M = 0.344$ V at $V_{DD} = 0.7$ V, see Table S4 in the Supporting Information), voltage gain over 100 V V^{-1}, $P_{static} < 2$ nW, and $P_{dynamic} < 2.2$ µW (Figure 5c–f and Tables S4 and S5, Supporting Information). These OECT-based complementary inverters are among the best reported sub-1 V CMOS-like technologies.[40] Thus, enhancing the charge transport properties of n-type OMIECs to match that of p-type OMIECs is the key to achieving high-performance complementary OECT circuits.

3. Conclusions

We have investigated the influence of molecular weight on charge transport properties and OECT performance of

**ADVANCED
SCIENCE NEWS**

www.advancedsciencenews.com

**ADVANCED
MATERIALS**

www.advmat.de

the ladder-type polymer BBL. We have demonstrated that increasing the molecular weight of BBL by one order of magnitude (from 4.9 to 51 kDa) yields n-type OECTs with record-high $g_{m,norm}$ (11.1 S cm^{-1}) and μC^* (25.9 F cm^{-1} V^{-1} s^{-1}). The improvement in OECT performance is ascribed to a strong π–π interaction and high crystallinity. As a result of the improved intermolecular charge transport, the reported OECTs have a fast transient response (0.38 ms) and low threshold voltage (0.15 V). By combining the best-performing BBL-based OECTs with P($g_4$2T-T)-based p-type OECTs, we demonstrated OECT-based complementary inverters with record-high voltage gain (up to 100 V V^{-1}) and ultralow power consumption (down to 0.32 nW), depending on the supply voltage. These devices are among the best-performing sub-1 V complementary inverters reported to date. This work provides a molecular design strategy to optimize the OECT performance of rigid OMIEC polymers and opens to a new generation of power-efficient organic (bio-)electronic devices.

4. Experimental Section

Materials: TABH, NDA, PPA, and MSA were purchased from Sigma-Aldrich. To remove the adsorbed moisture, NDA was washed with acetone then dried in the oven at 150 °C for 1 h, while TABH was dried in the oven at 150 °C for 10 min. Other reagents were used as received. BBL was synthesized following a procedure reported previously.[41] In brief, PPA (250 g) was added to a 500 mL three-necked flask fitted with an overhead stirrer and nitrogen inlet/outlet. The PPA was deoxygenated by heating overnight at 110 °C with nitrogen bubbling through the stirred acid. Then, 2.00 g (7.05 mmol) of TABH was added under a nitrogen atmosphere at 50 °C. The mixture was heated overnight at 75 °C, and NDA (1.89 g, 7.05 mmol) was then added. The mixture was slowly heated (4 °C min^{-1}) to 180 °C and maintained at that temperature for 2, 4, 12, or 48 h to obtain BBL$_{15}$, BBL$_{60}$, BBL$_{98}$, and BBL$_{152}$, respectively. The resulting viscous solution was poured out of the flask at 180 °C into a beaker and allowed to cool to room temperature. The polymer was precipitated in methanol, using a blender to facilitate mixing. The brown fibrous material was washed twice with methanol and water, and dried at 200 °C under reduced pressure (0.40 mm Hg). Precipitation from 500 g of MSA and drying in the above manner gave BBL as dark purple powders or fibers with metallic luster (2.10 g, 89% yield, η = 0.45 dL g^{-1} in MSA at 30 °C, M_v = 4.89 kDa, BBL$_{15}$; 2.18 g, 93% yield, η = 2.96 dL g^{-1} in MSA at 30 °C, M_v = 20.0 kDa, BBL$_{60}$; 2.16 g, 92% yield, η = 5.74 dL g^{-1} in MSA at 30 °C, M_v = 32.8 kDa, BBL$_{98}$; 2.24 g, 95% yield, η = 10.32 dL g^{-1} in MSA at 30 °C, M_v = 50.8 kDa, BBL$_{152}$). For M_v's estimation, the viscosity was measured with an Ubbelohde type viscometer, using K = 5.11 × 10^{-6} g dL^{-1} and α = 1.34.[42] P($g_4$2T-T) was synthesized following the procedure reported in ref. [43].

Thin-Film Casting: BBL$_{15}$, BBL$_{60}$, BBL$_{98}$, and BBL$_{152}$ were dissolved in MSA at 100 °C for 12 h then cooled down to room temperature to obtain BBL-MSA solution. The solution was spin-cast (1000 rpm, 60 s, acceleration 1000 rpm s^{-1}) on glass or Si/SiO$_2$ substrate. Then, the thin BBL films were immersed in deionized water to remove residual MSA and dried with nitrogen flow. The film thickness was controlled by the BBL-MSA solution concentration, typically 1–60 mg mL^{-1} for 20–200 nm film thickness. P($g_4$2T-T) was dissolved in 1,2-dichlorobenzene (ODCB) at 100 °C for 12 h to obtain P($g_4$2T-T)-ODCB solution with a concentration of 1 mg mL^{-1}. The solution was spin-cast (2000 rpm, 90 s, acceleration 2000 rpm s^{-1}) on a glass substrate to obtain P($g_4$2T-T) thin films. The film thickness was measured by AFM (Dimension 3100/Nanoscope IV system) and stylus profilometer (Bruker DektakXT Advanced System).

UV–Vis Absorption Spectra: Thin-film absorption spectra and spectroelectrochemistry measurements were performed on 200 nm

thick films of BBL$_{15}$, BBL$_{60}$, BBL$_{98}$, and BBL$_{152}$ on indium tin oxide glass substrate (0.85 cm × 3 cm). For spectroelectrochemistry measurements, the BBL thin films were grounded, and 0.1 M NaCl aqueous solution was used as the electrolyte, with the voltage applied to the Ag/AgCl pellet electrode through a Keithley 4200A-SCS. For each voltage step, a constant voltage was maintained for 200 s to ensure that the electrochemically doping reached a steady state. The absorption spectra were measured by Perkin-Elmer Lambda 900 spectrometer at 25 °C.

Electrochemistry: CV and electrochemical impedance spectroscopy (EIS) were performed on Potentiostat BioLogic SP-200. CV measurements were carried out in 0.1 M n-Bu$_4$NPF$_6$ anhydrous acetonitrile solution electrolyte (bubbling with nitrogen for 1 min to remove the dissolved oxygen before measures). 200 nm thick BBL thin films were spin-cast and patterned on chromium/gold (5 nm/50 nm) electrode (5 mm × 5 mm size) on a glass substrate, which served as the working electrode (WE). The counter electrode (CE) was a platinum wire and all potentials were recorded versus Ag/AgCl (saturated) as the reference electrode (RE). The scan rate was 50 mV s^{-1}. In EIS measurement, 0.1 M NaCl aqueous solution was used as the electrolyte, a platinum wire was used as the CE, Ag/AgCl (saturated) was used as the RE, and patterned BBL thin films with a volume of 8.1 × 10^{-7} to 5.1 × 10^{-5} cm^3 on Cr/Au electrode on glass substrate served as the WE. WE was set to −0.7 V for volumetric capacitance measurements, and spectra were recorded in the frequency range 0.1 Hz–10 kHz. The capacitance was extracted by fitting to modified Randles circuit model: R_s + CPE/(R_{ct} + M), where R_s is the active electrolyte resistance, CPE is a constant phase element, R_{ct} is the charge transfer resistance, and M is the restricted diffusion impedance.[44]

Dynamic Light Scattering: DLS measurements were performed at Zetasizer Nano ZS90 (laser wavelength λ = 632.8 nm) at T = 298 K. BBL$_{15}$, BBL$_{60}$, BBL$_{98}$, and BBL$_{152}$ were dissolved in MSA at 100 °C for 12 h then cooled down to room temperature and filtered through 0.45 μm polypropylene filter to obtain BBL-MSA solution. The scattering signal was measured at θ = 90° for 10 s and repeated 100 times. The decay rate (Γ) was calculated by fitting the first-order autocorrelation as $g^1(\tau) = B + A\exp(-\Gamma\tau)$. The apparent hydrodynamic diameter (D_h) was calculated through Stokes–Einstein relation $D_h = k_BT/3\pi\eta D$, diffusion coefficient $D = \Gamma/q^2$, and scattering vector $q = (4\pi n/\lambda)\sin(\theta/2)$. A solvent viscosity η_{MSA} = 11.7 mPa s, refractive index n_{MSA} = 1.429, and Boltzmann constant k_B = 1.38 × 10^{-23} m^2 kg s^{-2} K^{-1} were used in the above calculations.[45]

Grazing-Incidence Wide-Angle X-ray Scattering: GIWAXS experiments were performed at Beamline 9A at the Pohang Accelerator Laboratory in South Korea. The X-ray energy was 11.08 eV and the incidence angle was 0.12°. Samples were measured in vacuum and the total exposure time was 10 s. The scattered X-rays were recorded by a charge-coupled device detector located 221.9351 mm from the sample. All samples for GIWAXS measurements had a similar thickness of 100 nm.

OECTs and Complementary Inverters: OECTs were fabricated following a procedure reported previously.[46] Standard microscope glass slides were cleaned via successive sonication in acetone, deionized water, and isopropyl alcohol, and dried with nitrogen. Source/drain electrodes (5 nm Cr and 50 nm Au) were thermally deposited and photolithographically patterned by wet etching. A first layer of parylene C (4 μm), deposited together with a small amount of 3-(trimethoxysilyl) propyl methacrylate (A-174 Silane) to enhance adhesion, acted as an insulator to prevent disturbing capacitive effects at the metal liquid interface. Subsequently, a dilution of industrial surfactant (2% Decan-90) was spin-coated as an antiadhesive layer and a second layer of parylene C (4 μm) was deposited as a sacrificial layer. To protect the parylene C layers from a subsequent plasma reactive ion etching step (150 W, O$_2$ = 500 sccm, CF$_4$ = 1000 sccm, 510 s), a thick positive photoresist (10 μm, AZ10XT520CP) was spin-coated on the parylene C layer. A second photolithographic patterning step was carried out to define the contact pads and the OECT channel, and the AZ developer was applied to the photoresist. The subsequent plasma reactive ion etching step was used to indiscriminately remove the layer of organic materials, including both photoresist and parylene C, so that the contact pads and the OECT

channel area were exposed to the air while other areas were still covered with two layers of parylene C. The channel between source and drain were patterned to obtain $W/L = 20\ \mu m/10\ \mu m$ and $100\ \mu m/10\ \mu m$. BBL_{15}, BBL_{60}, BBL_{98}, and BBL_{152} MSA solutions were spin-coated to obtain 20 nm thick film, covering the whole substrate surface. The sacrificial layer was peeled off and the BBL film on it was removed, leaving separated pieces of film staying in the wells, consisting of the semiconductor connecting the OECT source/drain electrodes. $P(g_42T-T)$-based OECTs were fabricated using a similar procedure. For all OECTs, 0.1 M NaCl aqueous solution was used as the electrolyte and Ag/AgCl pellet electrode (purchased from VWR) was used as the gate electrode. The complementary inverters were assembled by connecting a $P(g_42T-T)$-based OECT and a BBL_{152}-based OECT using silver paint (Figure 5a). The OECTs and inverters were characterized by Keithley 4200A-SCS (with 4225-PMU Ultra Fast I-V Module and 4225-RPM Remote Amplifier/Switch Modules).

Supporting Information

Supporting Information is available from the Wiley Online Library or from the author.

Conflict of Interest

C.-Y.Y., M.-A.S., M.B., and S.F. are the co-founder of n-Ink AB. The other authors declare no competing interests.

Data Availability Statement

The data that support the findings of this study are available from the corresponding author upon reasonable request.

[1] B. D. Paulsen, K. Tybrandt, E. Stavrinidou, J. Rivnay, *Nat. Mater.* **2020**, *19*, 13.

[2] B. D. Paulsen, S. Fabiano, J. Rivnay, *Annu. Rev. Mater. Res.* **2021**, *51*, 73.

[3] I. Bargigia, L. R. Savagian, A. M. Osterholm, J. R. Reynolds, C. Silva, *J. Am. Chem. Soc.* **2021**, *143*, 294.

[4] a) S. van Reenen, R. A. J. Janssen, M. Kemerink, *Adv. Funct. Mater.* **2015**, *25*, 3066; b) S. Tang, A. Sandstrom, P. Lundberg, T. Lanz, C. Larsen, S. van Reenen, M. Kemerink, L. Edman, *Nat Commun.* **2017**, *8*, 1190; c) P. Lundberg, Y. Tsuchiya, E. M. Lindh, S. Tang, C. Adachi, L. Edman, *Nat. Commun.* **2019**, *10*, 5307.

[5] a) C. C. Yu, C. Y. Wang, X. Liu, X. T. Jia, S. Naficy, K. W. Shu, M. Forsyth, G. G. Wallace, *Adv. Mater.* **2016**, *28*, 9349; b) D. Moia, A. Giovannitti, A. A. Szumska, I. P. Maria, E. Rezasoltani, M. Sachs, M. Schnurr, P. R. F. Barnes, I. McCulloch, J. Nelson, *Energy Environ. Sci.* **2019**, *12*, 1349; c) A. V. Volkov, H. Sun, R. Kroon, T.-P. Ruoko, C. Che, J. Edberg, C. Muller, S. Fabiano, X. Crispin, *ACS Appl. Energy Mater.* **2019**, *2*, 5350; d) L. Manjakkal, A. Pullanchiyodan, N. Yogeswaran, E. S. Hosseini, R. Dahiya, *Adv. Mater.* **2020**, *32*, 1907254; e) H. M. Wang, Y. F. Diao, Y. Lu, H. R. Yang, Q. J. Zhou, K. Chrulski, J. M. D'Arcy, *Nat. Commun.* **2020**, *11*, 3882.

[6] a) E. Zeglio, A. L. Rutz, T. E. Winkler, G. G. Malliaras, A. Herland, *Adv. Mater.* **2019**, *31*, 1806712; b) E. Macchia, R. A. Picca, K. Manoli, C. Di Franco, D. Blasi, L. Sarcina, N. Ditaranto, N. Cioffi, R. Osterbacka, G. Scamarcio, F. Torricelli, L. Torsi, *Mater. Horiz.* **2020**, *7*, 999; c) R. A. Picca, K. Manoli, E. Macchia, L. Sarcina, C. Di Franco, N. Cioffi, D. Blasi, R. Osterbacka, F. Torricelli, G. Scamarcio, L. Torsi, *Adv. Funct. Mater.* **2020**, *30*, 1904513; d) X. Zhang, B. Wang, L. Huang, W. Huang, Z. Wang, W. Zhu, Y. Chen, Y. Mao, A. Facchetti, T. J. Marks, *Sci. Adv.* **2020**, *6*, eaaz1042.

[7] a) Z. Fan, J. Y. Ouyang, *Adv. Electron. Mater.* **2019**, *5*, 1800769; b) D. Scheunemann, V. Vijayakumar, H. Y. Zeng, P. Durand, N. Leclerc, M. Brinkmann, M. Kemerink, *Adv. Electron. Mater.* **2020**, *6*, 2000218.

[8] a) M. M. Ma, L. Guo, D. G. Anderson, R. Langer, *Science* **2013**, *339*, 186; b) K. R. Li, Y. L. Shao, H. P. Yan, Z. Lu, K. J. Griffith, J. H. Yan, G. Wang, H. W. Fan, J. Y. Lu, W. Huang, B. Bao, X. L. Liu, C. Y. Hou, Q. H. Zhang, Y. G. Li, J. S. Yu, H. Z. Wang, *Nat. Commun.* **2018**, *9*, 4798.

[9] J. Rivnay, S. Inal, A. Salleo, R. M. Owens, M. Berggren, G. G. Malliaras, *Nat. Rev. Mater.* **2018**, *3*, 17086.

[10] D. Khodagholy, J. Rivnay, M. Sessolo, M. Gurfinkel, P. Leleux, L. H. Jimison, E. Stavrinidou, T. Herve, S. Sanaur, R. M. Owens, G. G. Malliaras, *Nat. Commun.* **2013**, *4*, 2133.

[11] A. M. Pappa, D. Ohayon, A. Giovannitti, I. P. Maria, A. Savva, I. Uguz, J. Rivnay, I. McCulloch, R. M. Owens, S. Inal, *Sci. Adv.* **2018**, *4*, eaat0911.

[12] D. Khodagholy, T. Doublet, P. Quilichini, M. Gurfinkel, P. Leleux, A. Ghestem, E. Ismailova, T. Hervé, S. Sanaur, C. Bernard, G. G. Malliaras, *Nat. Commun.* **2013**, *4*, 1575.

[13] a) P. A. Ersman, R. Lassnig, J. Strandberg, D. Tu, V. Keshmiri, R. Forchheimer, S. Fabiano, G. Gustafsson, M. Berggren, *Nat. Commun.* **2019**, *10*, 5053; b) M. Zabihipour, R. Lassnig, J. Strandberg, M. Berggren, S. Fabiano, I. Engquist, P. A. Ersman, *npj Flexible Electron.* **2020**, *4*, 15.

[14] a) P. Gkoupidenis, D. A. Koutsouras, G. G. Malliaras, *Nat. Commun.* **2017**, *8*, 15448; b) Y. van de Burgt, E. Lubberman, E. J. Fuller, S. T. Keene, G. C. Faria, S. Agarwal, M. J. Marinella, A. Alec Talin, A. Salleo, *Nat. Mater.* **2017**, *16*, 414; c) J. Y. Gerasimov, R. Gabrielsson, R. Forchheimer, E. Stavrinidou, D. T. Simon, M. Berggren, S. Fabiano, *Adv. Sci.* **2019**, *6*, 1801339.

[15] a) D. Tu, S. Fabiano, *Appl. Phys. Lett.* **2020**, *117*, 080501; b) V. Kaphle, P. R. Paudel, D. Dahal, R. K. Radha Krishnan, B. Lüssem, *Nat. Commun.* **2020**, *11*, 2515.

[16] H. Sirringhaus, *Adv. Mater.* **2014**, *26*, 1319.

[17] J. Rivnay, P. Leleux, M. Ferro, M. Sessolo, A. Williamson, D. A. Koutsouras, D. Khodagholy, M. Ramuz, X. Strakosas, R. M. Owens, C. Benar, J.-M. Badier, C. Bernard, G. G. Malliaras, *Sci. Adv.* **2015**, *1*, e1400251.

[18] a) Y. Wang, E. Zeglio, H. Liao, J. Xu, F. Liu, Z. Li, I. P. Maria, D. Mawad, A. Herland, I. McCulloch, W. Yue, *Chem. Mater.* **2019**, *31*, 9797; b) P. Schmode, D. Ohayon, P. M. Reichstein, A. Savva, S. Inal, M. Thelakkat, *Chem. Mater.* **2019**, *31*, 5286; c) A. Savva, R. Hallani, C. Cendra, J. Surgailis, T. C. Hidalgo, S. Wustoni, R. Sheelamanthula, X. X. Chen, M. Kirkus, A. Giovannitti, A. Salleo, I. McCulloch, S. Inal, *Adv. Funct. Mater.* **2020**, *30*, 1907657; d) M. Moser, A. Savva, K. Thorley, B. D. Paulsen, T. C. Hidalgo, D. Ohayon, H. Chen, A. Giovannitti, A. Marks, N. Gasparini, A. Wadsworth, J. Rivnay, S. Inal, I. McCulloch, *Angew. Chem., Int. Ed.* **2021**, *60*, 7777; e) M. Moser, L. R. Savagian, A. Savva, M. Matta, J. F. Ponder, T. C. Hidalgo, D. Ohayon, R. Hallani, M. Reisjalali, A. Troisi, A. Wadsworth, J. R. Reynolds, S. Inal, I. McCulloch, *Chem. Mater.* **2020**, *32*, 6618; f) X. Luo, H. Shen, K. Perera, D. T. Tran, B. W. Boudouris, J. Mei, *ACS Macro Lett.* **2021**, *10*, 1061; g) A. T. Lill, D. X. Cao, M. Schrock, J. Vollbrecht, J. F. Huang, N. D. Tung, V. V. Brus, B. Yurash, D. Leifert, G. C. Bazan, T. Q. Nguyen, *Adv. Mater.* **2020**, *32*, 1908120; h) G. Krauss, F. Meichsner, A. Hochgesang, J. Mohanraj, S. Salehi, P. Schmode, M. Thelakkat, *Adv. Funct. Mater.* **2021**, *31*, 2010048; i) B. V. Khau, L. R. Savagian, M. De Keersmaecker, M. A. Gonzalez, E. Reichmanis, *ACS Mater. Lett.* **2019**, *1*, 599; j) A. L. Jones, M. De Keersmaecker, L. R. Savagian, B. T. DiTullio, I. Pelse, J. R. Reynolds, *Adv. Funct. Mater.* **2021**, *31*, 2102688; k) H. Y. Jia, Z. Huang, P. Y. Li, S. Zhang, Y. F. Wang, J. Y. Wang, X. D. Gu, T. Lei, *J. Mater. Chem. C* **2021**, *9*, 4927; l) C. Cea, G. D. Spyropoulos, P. Jastrzebska-Perfect, J. J. Ferrero, J. N. Gelinas, D. Khodagholy, *Nat. Mater.* **2020**, *19*, 679.

[19] A. Giovannitti, I. P. Maria, D. Hanifi, M. J. Donahue, D. Bryant, K. J. Barth, B. E. Makdah, A. Savva, D. Moia, M. Zetek, P. R. F. Barnes, O. G. Reid, S. Inal, G. Rumbles, G. G. Malliaras, J. Nelson, J. Rivnay, I. McCulloch, *Chem. Mater.* **2018**, *30*, 2945.

[20] X. Chen, A. Marks, B. D. Paulsen, R. Wu, R. B. Rashid, H. Chen, M. Alsufyani, J. Rivnay, I. McCulloch, *Angew. Chem., Int. Ed.* **2021**, *60*, 9368.

[21] A. F. Paterson, H. Faber, A. Savva, G. Nikiforidis, M. Gedda, T. C. Hidalgo, X. Chen, I. McCulloch, T. D. Anthopoulos, S. Inal, *Adv. Mater.* **2019**, *31*, 1902291.

[22] A. F. Paterson, A. Savva, S. Wustoni, L. Tsetseris, B. D. Paulsen, H. Faber, A. H. Emwas, X. Chen, G. Nikiforidis, T. C. Hidalgo, M. Moser, I. P. Maria, J. Rivnay, I. McCulloch, T. D. Anthopoulos, S. Inal, *Nat. Commun.* **2020**, *11*, 3004.

[23] C.-Y. Yang, M.-A. Stoeckel, T.-P. Ruoko, H.-Y. Wu, X. Liu, N. B. Kolhe, Z. Wu, Y. Puttisong, C. Musumeci, M. Massetti, H. Sun, K. Xu, D. Tu, W. M. Chen, H. Y. Woo, M. Fahlman, S. A. Jenekhe, M. Berggren, S. Fabiano, *Nat. Commun.* **2021**, *12*, 2354.

[24] A. Giovannitti, C. B. Nielsen, D.-T. Sbircea, S. Inal, M. Donahue, M. R. Niazi, D. A. Hanifi, A. Amassian, G. G. Malliaras, J. Rivnay, I. McCulloch, *Nat. Commun.* **2016**, *7*, 13066.

[25] a) S. Wang, H. Sun, T. Erdmann, G. Wang, D. Fazzi, U. Lappan, Y. Puttisong, Z. Chen, M. Berggren, X. Crispin, A. Kiriy, B. Voit, T. J. Marks, S. Fabiano, A. Facchetti, *Adv. Mater.* **2018**, *30*, 1801898; b) S. Wang, D. Fazzi, Y. Puttisong, M. J. Jafari, Z. Chen, T. Ederth, J. W. Andreasen, W. M. Chen, A. Facchetti, S. Fabiano, *Chem. Mater.* **2019**, *31*, 3395.

[26] a) S. Wang, H. Sun, U. Ail, M. Vagin, P. O. A. Persson, J. W. Andreasen, W. Thiel, M. Berggren, X. Crispin, D. Fazzi, S. Fabiano, *Adv. Mater.* **2016**, *28*, 10764; b) D. Fazzi, S. Fabiano, T.-P. Ruoko, K. Meerholz, F. Negri, *J. Mater. Chem. C* **2019**, *7*, 12876.

[27] H. Sun, M. Vagin, S. Wang, X. Crispin, R. Forchheimer, M. Berggren, S. Fabiano, *Adv. Mater.* **2018**, *30*, 1704916.

[28] J. Surgailis, A. Savva, V. Druet, B. D. Paulsen, R. Wu, A. Hamidi-Sakr, D. Ohayon, G. Nikiforidis, X. Chen, I. McCulloch, J. Rivnay, S. Inal, *Adv. Funct. Mater.* **2021**, *31*, 2010165.

[29] a) L. Zhang, N. S. Colella, F. Liu, S. Trahan, J. K. Baral, H. H. Winter, S. C. B. Mannsfeld, A. L. Briseno, *J. Am. Chem. Soc.* **2013**, *135*, 844; b) M. M. Nahid, R. Matsidik, A. Welford, E. Gann, L. Thomsen, M. Sommer, C. R. McNeill, *Adv. Funct. Mater.* **2017**, *27*, 1604744; c) D. K. Tran, A. Robitaille, I. J. Hai, X. Ding, D. Kuzuhara, T. Koganezawa, Y.-C. Chiu, M. Leclerc, S. A. Jenekhe, *J. Mater. Chem. A* **2020**, *8*, 21070.

[30] R. Noriega, J. Rivnay, K. Vandewal, F. P. V. Koch, N. Stingelin, P. Smith, M. F. Toney, A. Salleo, *Nat. Mater.* **2013**, *12*, 1038.

[31] R. J. Kline, M. D. McGehee, E. N. Kadnikova, J. S. Liu, J. M. J. Frechet, *Adv. Mater.* **2003**, *15*, 1519.

[32] J. Li, Y. Zhao, H. S. Tan, Y. Guo, C.-A. Di, G. Yu, Y. Liu, M. Lin, S. H. Lim, Y. Zhou, H. Su, B. S. Ong, *Sci. Rep.* **2012**, *2*, 754.

[33] a) S. A. Jenekhe, P. O. Johnson, *Macromolecules* **1990**, *23*, 4419; b) M. Mamada, C. Perez-Bolivar, D. Kumaki, N. A. Esipenko, S. Tokito, P. Anzenbacher, *Chem. – Eur. J.* **2014**, *20*, 11835; c) S. Erten, S. Icli, *Inorg. Chim. Acta* **2008**, *361*, 595.

[34] a) C. J. Collison, L. J. Rothberg, V. Treemaneekarn, Y. Li, *Macromolecules* **2001**, *34*, 2346; b) T. Lei, J. H. Dou, J. Pei, *Adv. Mater.* **2012**, *24*, 6457.

[35] Z.-Y. Wang, L. Di Virgilio, Z.-F. Yao, Z.-D. Yu, X.-Y. Wang, Y.-Y. Zhou, Q.-Y. Li, Y. Lu, L. Zou, H. I. Wang, X.-Y. Wang, J.-Y. Wang, J. Pei, *Angew. Chem., Int. Ed.* **2021**, *60*, 20483.

[36] S. H. Wang, T. P. Ruoko, G. Wang, S. Riera-Galindo, S. Hultmark, Y. Puttisong, F. Moro, H. P. Yan, W. M. Chen, M. Berggren, C. Muller, S. Fabiano, *ACS Appl. Mater. Interfaces* **2020**, *12*, 53003.

[37] S. Inal, G. G. Malliaras, J. Rivnay, *Nat. Commun.* **2017**, *8*, 1767.

[38] C.-Y. Yang, D. Tu, T.-P. Ruoko, J. Y. Gerasimov, H.-Y. Wu, P. C. Harikesh, R. Kroon, C. Müller, M. Berggren, S. Fabiano, *arXiv:2106.07438*, **2021**.

[39] A. Giovannitti, D.-T. Sbircea, S. Inal, C. B. Nielsen, E. Bandiello, D. A. Hanifi, M. Sessolo, G. G. Malliaras, I. McCulloch, J. Rivnay, *Proc. Natl. Acad. Sci. U. S. A.* **2016**, *113*, 12017.

[40] a) M. H. Alam, Z. F. Xu, S. Chowdhury, Z. Z. Jiang, D. Taneja, S. K. Banerjee, K. J. Lai, M. H. Braga, D. Akinwande, *Nat. Commun.* **2020**, *11*, 3203; b) P. Romele, P. Gkoupidenis, D. A. Koutsouras, K. Lieberth, Z. M. Kovacs-Vajna, P. W. M. Blom, F. Torricelli, *Nat. Commun.* **2020**, *11*, 3743; c) A. G. Shulga, V. Derenskyi, J. M. Salazar-Rios, D. N. Dirin, M. Fritsch, M. V. Kovalenko, U. Scherf, M. A. Loi, *Adv. Mater.* **2017**, *29*, 1701764; d) U. Zschieschang, V. P. Bader, H. Klauk, *Org. Electron.* **2017**, *49*, 179.

[41] F. E. Arnold, R. L. V. Deusen, *Macromolecules* **1969**, *2*, 497.

[42] a) G. Berry, S. Yen, in *Addition and Condensation Polymerization Processes*, Vol. *91* (Ed: N. A. J. Platzer), American Chemical Society, Washington, DC, USA **1969**, p. 734; b) C. P. Wong, H. Ohnuma, G. C. Berry, *J. Polym. Sci., Part C: Polym. Symp.* **1978**, *65*, 173.

[43] a) R. Kroon, D. Kiefer, D. Stegerer, L. Yu, M. Sommer, C. Mueller, *Adv. Mater.* **2017**, *29*, 1700930; b) D. Kiefer, R. Kroon, A. I. Hofmann, H. D. Sun, X. J. Liu, A. Giovannitti, D. Stegerer, A. Cano, J. Hynynen, L. Y. Yu, Y. D. Zhang, D. Q. Nai, T. F. Harrelson, M. Sommer, A. J. Moule, M. Kemerink, S. R. Marder, I. McCulloch, M. Fahlman, S. Fabiano, C. Muller, *Nat. Mater.* **2019**, *18*, 149.

[44] J. Bisquert, A. Compte, *J. Electroanal. Chem.* **2001**, *499*, 112.

[45] A. I. Hofmann, D. Katsigiannopoulos, M. Mumtaz, I. Petsagkourakis, G. Pecastaings, G. Fleury, C. Schatz, E. Pavlopoulou, C. Brochon, G. Hadziioannou, E. Cloutet, *Macromolecules* **2017**, *50*, 1959.

[46] M. Braendlein, T. Lonjaret, P. Leleux, J. M. Badier, G. G. Malliaras, *Adv. Sci.* **2017**, *4*, 1600247.

[47] C. G. Bischak, L. Q. Flagg, K. R. Yan, C. Z. Li, D. S. Ginger, *ACS Appl. Mater. Interfaces* **2019**, *11*, 28138.

[48] M. Kawan, T. C. Hidalgo, W. Y. Du, A. M. Pappa, R. M. Owens, I. McCulloch, S. Inal, *Mater. Horiz.* **2020**, *7*, 2348.

[49] I. P. Maria, B. D. Paulsen, A. Savva, D. Ohayon, R. H. Wu, R. Hallani, A. Basu, W. Y. Du, T. D. Anthopoulos, S. Inal, J. Rivnay, I. McCulloch, A. Giovannitti, *Adv. Funct. Mater.* **2021**, *31*, 2008718.

[50] D. Ohayon, A. Savva, W. Du, B. D. Paulsen, I. Uguz, R. S. Ashraf, J. Rivnay, I. McCulloch, S. Inal, *ACS Appl. Mater. Interfaces* **2021**, *13*, 4253.

[51] J. J. Samuel, A. Garudapalli, A. A. Mohapatra, C. Gangadharappa, S. Patil, N. P. B. Aetukuri, *Adv. Funct. Mater.* **2021**, *31*, 2102903.